

Shear-induced migration of a suspension under quasi-planar confinement

John T. Antolik¹, Amanda Howard², Fernando Vereda³, Nikolay Ionkin¹, Martin Maxey⁴ and Daniel M. Harris¹†

¹School of Engineering, Brown University, Providence, Rhode Island 02912, USA

²Pacific Northwest National Laboratory, Richland, WA, 99354, USA

³Applied Physics Department, Faculty of Sciences, University of Granada, Granada, Spain

⁴Division of Applied Mathematics, Brown University, Providence, Rhode Island 02912, USA

(Received xx; revised xx; accepted xx)

The shear-induced migration of a non-Brownian suspension of spherical particles in a Newtonian fluid is studied experimentally. The suspension is confined in a thin rectangular channel that prevents complete particle overlap and subjected to an oscillatory pressure-driven flow. Despite the significant confinement, the suspension exhibits many of the characteristic features of shear-induced migration in bulk suspensions. Furthermore, as a consequence of the channel geometry and the development and application of a single-camera particle tracking method, three-dimensional particle trajectories are obtained that allow us to directly associate particle contacts with the observed migration.

1. Introduction

Suspension flows of spherical particles in a Newtonian fluid pertain to a wide range of applications, including biomedical, industrial, and geographical. Such flows represent generally chaotic dynamical systems (Drazer *et al.* 2002), with the particles undergoing irreversible migration from an initial configuration to a final, steady state configuration.

The role of particle contacts and surface roughness in non-Brownian suspensions is a topic of current interest as it relates to the particles' irreversible migration in a shear flow. Particle surface roughness results in an inherent irreversibility in the particles' relative motion as the particles are displaced across streamlines, and also modifies the pair distribution function between particles (Rampall *et al.* 1997; Blanc *et al.* 2011; Ingber *et al.* 2006). It has been shown that neither the long-range hydrodynamic interactions (Metzger & Butler 2010) nor the lubrication forces (Metzger *et al.* 2013) contribute significantly to the irreversibility. However, the particle surface roughness plays a key role (Pham *et al.* 2015; Corte *et al.* 2008). Pine *et al.* (2005) discovered that there is a critical strain amplitude for a given volume fraction below which the particle locations are reversible in oscillating flow. Above this critical strain amplitude, chaos sets in. Pham *et al.* (2016) found that smoother particles lead to a higher critical strain amplitude and predicted the critical strain as a function of the particle surface roughness. The critical strain amplitude has been further explored in flows with clouds of particles in an oscillating shear flow. The clouds are shown to extend until the volume fraction is less than the critical volume fraction for irreversibility at a given strain amplitude (Metzger & Butler 2012; Howard & Maxey 2018).

Information about suspension flows comes from simulations and experiments. Simulations are costly, and quantities such as the particle surface roughness are represented

† Email address for correspondence: daniel_harris3@brown.edu

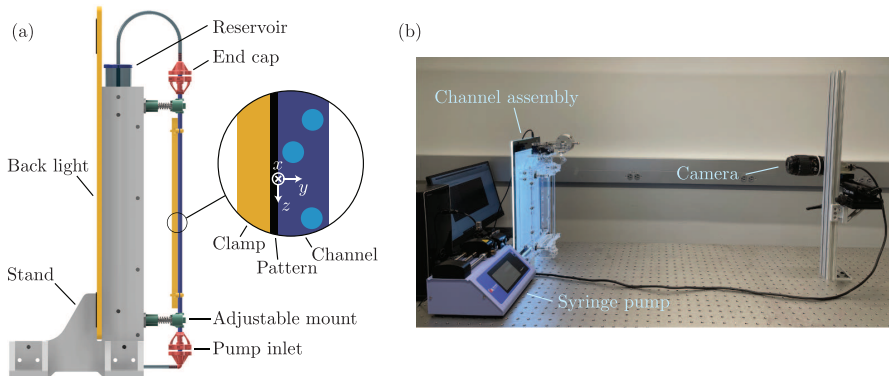


FIGURE 1. (a) A diagram of the channel assembly, along with a magnified view of the rectangular glass channel and speckle pattern positioning. Channel cross-section is 3 mm (y -direction) \times 9 mm (x -direction). (b) A photograph of the complete experimental setup.

by approximations such as an interparticle contact barrier. While simulations have been shown to accurately capture experiments (Maxey 2017), there is still a need for highly resolved experiments that can track particle locations. A number of experiments have been performed (Snook *et al.* 2015; Guasto *et al.* 2010; Pham *et al.* 2016) that use a laser sheet to image a slice of the suspension. This technique requires the suspending fluid to be index-matched to the particles and complete trajectories are unavailable because particles are lost from view once they leave the laser plane. Laser-Doppler velocimetry (LDV) has also been used to achieve high-resolution measurements of particle velocity and concentration (Lyon & Leal 1998*a,b*) but the one-dimensional nature of LDV prohibits simultaneous capture of the entire flow. Magnetic resonance imaging (MRI) can provide 3D measurements of suspensions which are optically opaque and hence is well suited to suspensions in porous media (Mirbod & Shapley 2023). However, individual particles cannot be tracked due to the relatively low resolution of MRI.

In this work, we study the migration of particles suspended in a viscous fluid subjected to an oscillatory pressure driven flow. Extended 3D particle trajectories are resolved with a single camera as a result of the quasi-planar channel geometry and refraction-based imaging technique capable of capturing particle motion in the out-of-plane direction. We report measurements of the migration dynamics for different packing fractions and strain amplitudes, and track interparticle contacts which are generally understood to be the source of irreversibility.

2. Experiments

The particles used in our experiments are optically clear acrylic (PMMA) spheres with diameter 1.598 ± 0.009 mm and root mean square surface roughness 0.08 ± 0.03 μm . They are suspended in a water-glycerol mixture with Newtonian viscosity 36.3 ± 1.8 cP (Cheng 2008) filling a 300 mm long Borosilicate glass test channel (VitroCom R0309, rectangular internal cross section 9×3 mm). The 3 mm channel height is just less than two particle diameters, preventing complete particle overlap.

The complete experimental setup is shown in figure 1. The glass test channel is oriented vertically and attached to a laser cut stand by screw-adjustable mounts. 3D-printed end caps with flow orifices ensure the particles remain in the channel and adapt the ends of the channel to hoses. The upper hose goes to a reservoir of suspending fluid which is open to the atmosphere and the bottom hose attaches to a syringe pump (Harvard Apparatus Pump 11 Elite).

TABLE 1. Relevant parameters and their range of values in our experimental study.

Parameter	Symbol	Definition	Value
Channel width	w	–	9 mm
Channel height	h	–	3 mm
Particle diameter	$2a$	–	1.598 ± 0.009 mm
Particle RMS roughness	–	–	0.08 ± 0.03 μm
Particle/fluid density	ρ	–	1.179 ± 0.003 g/mL
Fluid kinematic viscosity	μ	–	36.3 ± 1.8 cP
Strain amplitude	γ	$QT/w^2h = \langle u_z \rangle T/w$	1 - 6
Accumulated strain	γ_a	$2Qt/w^2h = 2\langle u_z \rangle t/w$	550 - 1100
Bulk volume fraction	ϕ_B	–	0.2 - 0.4
Volumetric flow rate	Q	$\langle u_z \rangle wh$	1 ± 0.005 mL/min
Particle diffusion coefficient	D	$kT_{\text{abs}}/(6\pi\mu a)$	7.4×10^{-18} m ² /s
Particle Reynolds number	Re	$\rho Qa/(wh\mu)$	1.6×10^{-2}
Peclet number	Pe	$aQ/(whD)$	8.8×10^{11}

A back light panel (3W LED tracing pad) illuminates the test section. We generate speckle patterns using the Rosta algorithm implementation (dot size 1, density 0.3 and zero smoothing) in the μDIC Python library (Olufsen *et al.* 2019) which are then ink-jet printed with 1200 x 2400 DPI resolution on transparency film. The pattern is fastened to the channel with a transparent acrylic clamping block. An Allied Vision Mako 503B monochrome CMOS camera with 105 mm micro Nikkor lens is used for imaging the suspension at a 1 Hz frame rate and 2592×610 resolution. The camera is placed at a working distance of approximately 1 m, resulting in a 40 mm by 10 mm imaged section. Hence lens distortion is minimized and the incident rays from the camera can be assumed to be parallel. The outlets of the channel are 130 mm away from the imaged section so entry length effects can be neglected.

We prepare particle suspensions with bulk particle volume fractions $\phi_B = 0.2, 0.3$ and 0.4. A magnetic 3D-printed plow-shaped particle pusher is used to manually set the initial particle distribution in the channel by guiding it with a handheld magnet outside the channel. The geometry of the pusher is such that the particles are driven to the channel walls in the x direction and the channel center ($y = h/2$) in the y direction. However, we observe that the particles quickly migrate towards the walls along the y direction once the experiment starts.

During the experiment, the syringe pump generates oscillatory flow in a square wave, prescribing the volumetric flow rate Q to be

$$Q(t) = \frac{\gamma w^2 h}{T} \frac{\sin(2\pi t/T)}{|\sin(2\pi t/T)|}, \quad (2.1)$$

where T is the flow oscillation period. The strain amplitude γ is the average displacement of a fluid parcel over a half cycle $T/2$ divided by the channel half width $w/2$. We perform experiments with $\gamma = 6$ up to an accumulated strain of 550 (46 oscillation cycles) and with $\gamma = 1$ to an accumulated strain of 1100 (550 oscillation cycles). The period T is chosen to maintain a particle Reynolds number of 0.016. Initial experiments performed at a Reynolds number of 0.008 produced indistinguishable suspension dynamics. Experiments were also performed with a single particle in the channel showing fully reversible motion in 3D, regardless of its initial position.

Prior to each experiment, a particle-free reference image of the speckle pattern is taken. Then, throughout the experiment, a series of photographs of the test section with particles

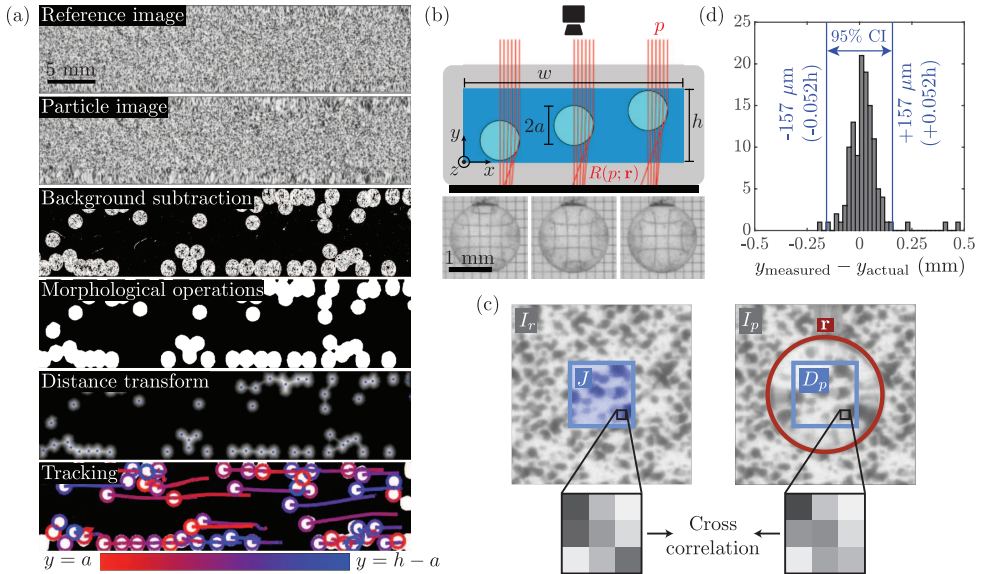


FIGURE 2. (a) Example images of the channel test section at each step of the processing procedure. The coloring of the tails in the “tracking” frame indicates each particle’s y position over time. (b) Cross-sectional diagram of the channel labelled with relevant dimensions. Incident rays from the camera at p are propagated based on the refraction model to $R(p; \mathbf{r})$ for particles at different heights. Experimental images of particles over a regular $200 \mu\text{m}$ grid pattern at the different heights shown below. (c) The reference image I_r is transformed based on the refraction model and the guessed particle position \mathbf{r} . The result in J is compared to the corresponding region D_p in the particle image I_p using the cross correlation. (d) Histogram of particle height measurement errors from 120 data points taken at 12 evenly spaced known positions in y .

are captured. Figure 2(a) outlines the image processing steps which include background subtraction (Zivkovic 2004), filtering with morphological operations, and determining 2D particle positions with the Euclidean distance transform and h-maxima filter (Vincent 1993). The out-of-plane y -component of each particle’s position may be inferred by comparing the reference and particle images since the speckle pattern in the particle image will be distorted depending on the particles’ positions. Figure 2(b) illustrates the working principle of this particle tracking technique. The incident rays from the camera refract at the fluid-particle interfaces and focus as they reach the pattern attached to the outside of the channel. As seen in the photographs corresponding to each particle height, increasing the y component of the particle position has the approximate effect of increasing the magnification of the pattern. By applying Snell’s law at each optical interface in this axisymmetric geometry (Hecht 2012), an analytical expression may be constructed which predicts the observed distortion of the reference pattern through the transparent particle. For the case of partially overlapping particles, the distortion is determined numerically by recursively propagating each incident ray from the camera through the cluster of particles until it reaches the speckle pattern. The particle’s position is then determined by solving the inverse problem illustrated in 2(c): given a reference image I_r of the pattern and the resulting particle image I_p , we find a position \mathbf{r} for the particle that reproduces the observed distortion by maximizing the cross correlation between regions J and D_p . We use the Nelder-Mead algorithm (Nelder & Mead 1965) in the NLOpt library (Johnson 2021) to optimize the cross correlation. The OpenCV library (Bradski 2000) for C++ is used to implement the image transformations and cross correlations. We validate the 3D tracking method by moving a single particle to known

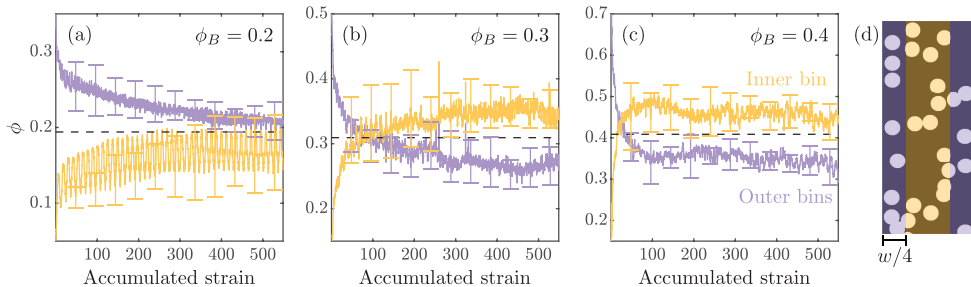


FIGURE 3. The evolution of particle concentration in the inner and outer bins is shown for (a) $\phi_B = 0.2$, (b) $\phi_B = 0.3$ and (c) $\phi_B = 0.4$; $\gamma = 6$. The dashed line indicates the bulk area fraction in the field of view averaged over the experiment. (d) The outer bins are one quarter of the channel width and the concentrations are calculated from the binary image as the number of white pixels divided by the number of total pixels in the bin.

positions in the channel with a translation stage and comparing with the refraction-based position measurement. Using a number of different particles at various locations in the field of view, the comparison between the measured height and the actual height reveals excellent agreement (figure 2(d)). Over the full measurement range, the particle’s y position can be determined to within $157 \mu\text{m}$ or 5.23% of the channel height with 95% confidence. The final processing step is to link the 3D particle positions into trajectories using Crocker and Grier’s algorithm (Crocker & Grier 1996) in the open-source library TrackPy (Allan *et al.* 2021) so that each particle’s identity is known throughout multiple frames, with the result shown in the “tracking” panel of figure 2(a).

3. Results

Examining the evolution of the local particle area fraction ϕ as a function of accumulated strain γ_a gives insight into the dynamics of the migration process and its dependence on bulk packing fraction. The average particle concentrations in the center and outer quarter-width bins when $\gamma = 6$ are plotted against the accumulated strain in figure 3. The results in these and all subsequent plots are averaged over at least 5 trials, with error bars representing one standard deviation. Due to the initial configuration of the particles, the initial outer bin concentration exceeds the bulk packing fraction for all experiments. However, for the $\phi_B = 0.3$ and $\phi_B = 0.4$ experiments, the inner and outer bin concentrations eventually cross and, at high accumulated strain, the inner bin concentration exceeds the bulk packing due to particle migration. Migration proceeds at an increased rate for $\phi_B = 0.4$. For the low packing fraction experiments with $\phi_B = 0.2$, the bin concentrations do not cross the average channel concentration up to an accumulated strain of 550, indicating a sharp reduction in the rate of migration. The oscillations in the inner bin concentration in figure 3(a) match the period of the flow and occur due to small variations in the packing fraction along the length of the channel.

The initial and steady state particle concentration profiles over the channel width are shown in figure 4(a) for experiments with $\gamma = 6$. Since the experiments begin in a wall-loaded configuration, the initial concentration profiles contain two peaks that are approximately one particle radius away from the channel walls. For the $\phi_B = 0.3$ and $\phi_B = 0.4$ experiments, the steady state concentration profiles indicate significant migration towards the channel center since the bulk packing fraction is surpassed there. However, compared against results with a parabolic flow profile in Snook *et al.* (2015) and

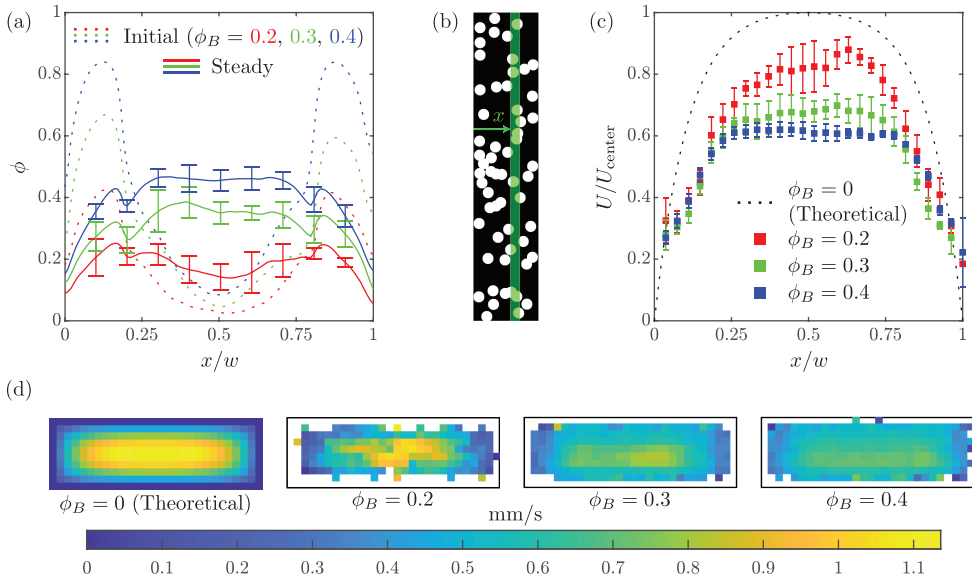


FIGURE 4. (a) Initial and steady state concentration profiles for $\gamma = 6$. Initial profiles were averaged over the first 20 frames ($\gamma_a < 2.74$) and steady profiles over frames 3500 to 3700 ($\gamma_a = [480, 508]$). (b) A bin is swept over the binary image in x to measure local concentration. (c) Center-line ($y = h/2$) particle velocity profiles compared to theoretical Newtonian case. (d) Cross-sectional particle velocity profiles.

Lyon & Leal (1998*a*), the concentration peak at the channel center is less pronounced, mirroring the flatter velocity profile in the current geometry. For $\phi_B = 0.2$, the particle arrangement relaxes from its initial configuration suggesting some irreversible behavior but there is less preferential migration towards the center of the channel. The particle concentration profiles are computed by sweeping a bin of one pixel width in single pixel increments over the binary particle image as shown in figure 4(b) and taking the local concentration as the number of white pixels in the bin divided by the number of black pixels. For clarity, error bars are shown at discrete points rather than at every pixel.

Enabled by the 3D particle tracking, figure 4(d) shows the average magnitude of the particle velocity over the channel cross section. The experimental velocity profiles are time-averaged over a full experiment and the theoretical velocity is calculated for a pure Newtonian fluid in Stokes flow. The white cells in the experimental profiles are regions where no velocity measurement could be obtained since the particle centers must be at least one particle radius away from the channel walls. For the $\phi_B = 0.2$ case, the magnitude of the measured velocity profile is close to the theoretical profile but the particle velocities are reduced for the higher packing cases. The mid-line particle velocity profiles at $y = h/2$ are compared in figure 4(c) against the theoretical center-line velocity. The profile becomes increasingly blunt with higher ϕ_B , consistent with results in a circular pipe (Snook *et al.* 2015) and two-dimensional channel flow (Lyon & Leal 1998*a*).

The mean square particle displacements (MSD) are a quantitative measure of irreversibility in the particles' motion and thus allow more detailed comparison between the experiments. The non-dimensional effective particle diffusivity D_x is defined following Pine *et al.* (2005) according to

$$\langle (\Delta x / (2a))^2 \rangle = 2D_x \gamma_a \quad (3.1)$$

where $\langle (\Delta x / (2a))^2 \rangle$ is the non-dimensional MSD, $2a$ is the particle diameter, γ_a is the

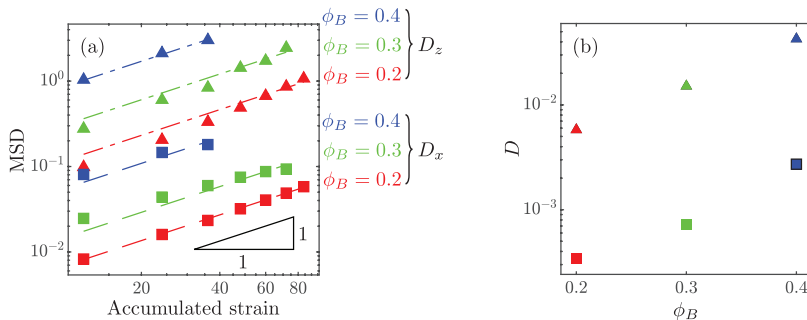


FIGURE 5. (a) Mean squared particle displacements in x and z for $\gamma = 6$. The dashed lines show linear fits to the data used to extract the effective diffusivities via equation (3.1). (b) Comparison of effective diffusivities D_x (squares) and D_z (triangles) at different bulk volume fractions.

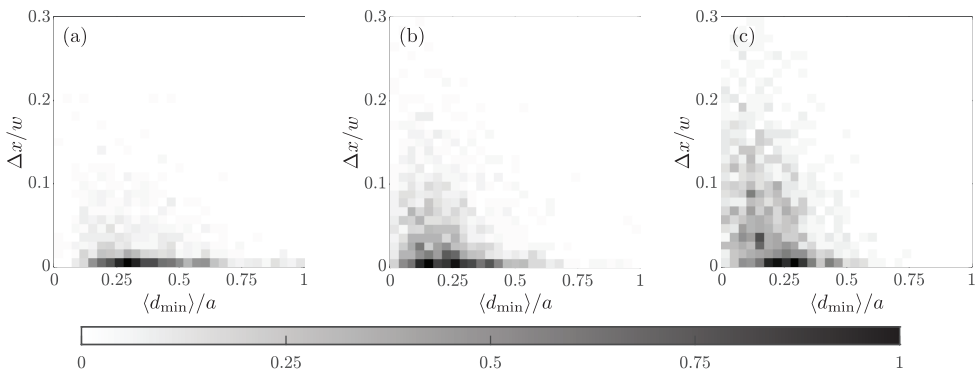


FIGURE 6. Heat maps of transverse particle migration over one cycle versus average distance to nearest neighbor at $\gamma = 6$ for (a) $\phi_B = 0.2$, (b) $\phi_B = 0.3$ and (c) $\phi_B = 0.4$. The color map is normalized by the maximum bin count which is 56, 57 and 32, respectively.

total accumulated strain and Δx is the displacement of the particle over one cycle. Given the three-dimensional nature of the flow geometry, effective diffusivities D_y and D_z for the other directions are defined in a similar manner. In order to ensure that the results are statistically significant, MSDs are computed up to the maximum accumulated strain for which there are at least 50 continuous particle trajectories (starting at any point in the experiment). Since higher bulk packing fraction increases the likelihood that a particle is lost during tracking, MSDs are calculated to a lower accumulated strain for higher ϕ_B experiments. The MSDs after an integral number of cycles in the $\gamma = 6$ experiments are graphed against the accumulated strain in figure 5(a). The y component is omitted as it does not exhibit diffusive behavior, presumably due to the high confinement. The least squares fits for the effective particle diffusivities are shown as well. For a given packing fraction, the effective diffusivity along the flow direction D_z is significantly higher than the transverse diffusivity D_x . This result is consistent with the findings in Pine *et al.* (2005) with a circular Couette flow where two components of diffusivity were measured. Guasto *et al.* (2010) also report that the streamwise diffusivity is consistently higher than the spanwise diffusivity in a rectangular channel flow. Figure 5(b) compares the effective diffusivities as a function of ϕ_B . For every value of ϕ_B , the ratio between D_x and D_z is about 20 but their values increase approximately one order of magnitude as ϕ_B increases from 0.2 to 0.4. The increase of effective diffusivity with bulk volume

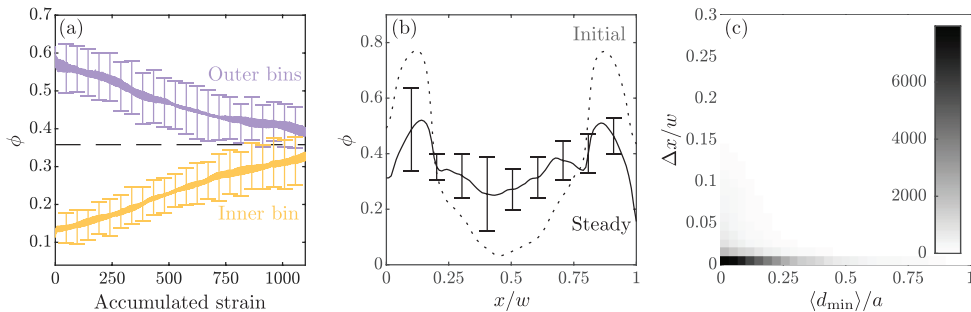


FIGURE 7. Experiments are performed at $\phi_B = 0.3$ and $\gamma = 1$ and the (a) bin concentration evolution, (b) concentration profiles and (c) migration heat map are plotted. The initial concentration profile is averaged over the first 20 frames ($\gamma_a < 2.74$) and the steady profile over frames 7000 to 7400 ($\gamma_a = [960, 1016]$).

fraction is consistent with experimental results in the literature for other flow geometries (Pine *et al.* 2005; Guasto *et al.* 2010).

Since the 3D position of each particle in the experiment is known, interactions between particles and the resulting irreversibility may be directly examined. Figure 6 shows the number of particles that migrate a given amount based on their proximity to their neighbors over a cycle. A particle’s level of interaction is quantified by $\langle d_{\min} \rangle/a$ which represents the average distance between a particle and its nearest neighbor over a cycle, normalized by the particle radius. For all experiments, the particles with more interactions have a greater tendency to migrate and as the packing fraction increases, so does the number of particles which interact closely with their neighbors. For the $\phi_B = 0.2$ experiments, there are few particles with $\langle d_{\min} \rangle/a < 0.2$ compared to the $\phi_B = 0.3$ or $\phi_B = 0.4$ experiments and consequently little migration towards the channel center, which is corroborated in the concentration profile results. Example videos of particle behavior at specific points on the heat map are provided in the supplementary materials.

Experiments are also performed at $\phi_B = 0.3$ and $\gamma = 1$ in order to observe the influence of strain amplitude on the migration dynamics. The average particle concentrations in the center and outer quarter-width bins are plotted against the accumulated strain in figure 7(a) up to an accumulated strain of 1100. Despite the large accumulated strain, the bin concentrations do not cross and the experiments exhibit quasi-reversible behavior where the bin concentrations change very slowly, potentially due to the effects of micro-buoyancy (due to distribution in particle density) which become more apparent on long timescales. The initial and steady state concentration profiles in figure 7(b) feature a similar lack of migration which is consistent with observations in the literature (Pham *et al.* 2016; Guasto *et al.* 2010) of a critical strain amplitude below which the particles can subtly reorganize into a configuration that is essentially reversible. For the migration heat map in figure 7(c), the peak intensity occurs near $\langle d_{\min} \rangle/a = 0$ yet almost no migration occurs. Since the suspension is quasi-reversible at this low strain amplitude, the particles remain near their initial tightly packed wall-loaded configuration.

4. Conclusions

In our experiments, suspensions of neutrally buoyant spherical particles at bulk volume fractions ϕ_B from 0.2 to 0.4 are subjected to oscillatory pipe flow in a confined rectangular channel and the resulting shear-induced migration is characterized through direct imaging. In experiments performed at strain amplitude $\gamma = 6$, the particles

are observed to migrate preferentially towards the channel center, with higher bulk volume fraction hastening the dynamics. These findings are consistent with results in the literature for other, unconfined flow geometries. Other measurements of the collective particle behavior such as local particle concentration and velocity are similarly consistent with previous results. The particle concentration profile achieves higher peaks at the channel center as the bulk volume fraction is increased. Conversely, the velocity profile is increasingly blunted compared to the theoretical $\phi_B = 0$ case as ϕ_B is increased. Additional experiments at a lower strain amplitude $\gamma = 1$ produce quasi-reversible particle behavior consistent with the existence of a critical strain amplitude below which shear migration does not occur (Pham *et al.* 2016).

We also implement a new, single-camera 3D particle tracking method. The transparent particles are imaged above a speckle pattern and the magnitude of the resulting optical distortions are used to infer the out-of-plane particle positions with high accuracy. This method trades the high optical component cost of typical shear-migration setups for computational complexity, utilizing a refraction model to predict the distortion of the speckle patterns and iterating the particle position to reproduce the observed distortion.

The 3D tracking method permits the characterization of not only collective, but also individual particle behavior, enabling direct observations of particle contacts and trajectories over long times. Consequently, it is possible to build a quantitative connection between particle interactions and displacement over a cycle to explain the source of migration. It is observed that, as bulk volume fraction increases, a greater number of particles experience close interactions with their neighbors and these same particles are responsible for the strongest individual migration events.

In addition to allowing measurements of otherwise inaccessible quantities in the mono-disperse case, our 3D tracking method has the advantage of convenient extension to the case of bi-disperse or poly-disperse suspensions as particle size can be easily determined during the optical reconstruction. Due to the presence of the channel walls which prevent particle overlap, the present experimental findings are also relevant to natural problems involving particle suspension in high confinement such as thin films (Hooshanginejad *et al.* 2019) or porous media (Mirbod & Shapley 2023).

Supplementary material. Supplementary videos are made available to the interested reader.

Funding. AH acknowledges support from the U.S. Department of Energy, Advanced Scientific Computing Research program, under the Scalable, Efficient and Accelerated Causal Reasoning Operators, Graphs and Spikes for Earth and Embedded Systems (SEA-CROGS) project, FWP 80278. Pacific Northwest National Laboratory (PNNL) is a multi-program national laboratory operated for the U.S. Department of Energy (DOE) by Battelle Memorial Institute under Contract No. DE-AC05-76RL01830. FV acknowledges funding from the University of Granada through the Brown/CASA-UGR Research Collaboration Fund and MICINN PID2019-104883GB-I00 project (Spain).

Code and data accessibility. Particle tracking code, associated documentation, and data sets can be found at <https://github.com/harrislab-brown/ParticleHeight>.

Declaration of interests. The authors report no conflict of interest.

REFERENCES

- ALLAN, D. B., CASWELL, T., KEIM, N. C., VAN DER WEL, C. M. & VERWEIJ, R. W. 2021 soft-matter/trackpy: Trackpy v0.5.0.
- BLANC, F., PETERS, F. & LEMAIRE, E. 2011 Experimental signature of the pair trajectories of rough spheres in the shear-induced microstructure in noncolloidal suspensions. *Physical Review Letters* **107** (20), 208302.

- BRADSKI, G. 2000 The OpenCV Library. *Dr. Dobb's Journal of Software Tools* .
- CHENG, N. S. 2008 Formula for viscosity of glycerol-water mixture. *Industrial and Engineering Chemistry Research* **47**, 3285–3288.
- CORTE, L., CHAIKIN, P. M., GOLLUB, J. P. & PINE, D. J. 2008 Random organization in periodically driven systems. *Nature Physics* **4** (5), 420–424.
- CROCKER, J. C. & GRIER, D. G. 1996 Methods of digital video microscopy for colloidal studies. *Journal of Colloid and Interface Science* **179** (1), 298–310.
- DRAZER, G., KOPLIK, J., KHUSID, B. & ACRIVOS, A. 2002 Deterministic and stochastic behaviour of non-Brownian spheres in sheared suspensions. *Journal of Fluid Mechanics* **460**, 307–335.
- GUASTO, J. S., ROSS, A. S. & GOLLUB, J. P. 2010 Hydrodynamic irreversibility in particle suspensions with nonuniform strain. *Physical Review E* **81**, 061401.
- HECHT, E. 2012 *Optics*. Pearson.
- HOOSHANGINEJAD, A., DRUECKE, B. C. & LEE, S. 2019 Stability analysis of a particle band on the fluid–fluid interface. *Journal of Fluid Mechanics* **869**.
- HOWARD, A. A. & MAXEY, M. R. 2018 Simulation study of particle clouds in oscillating shear flow. *Journal of Fluid Mechanics* **852**, 484–506.
- INGBER, M. S., MAMMOLI, A. A., VOROBIEFF, P., MCCOLLAM, T. & GRAHAM, A. L. 2006 Experimental and numerical analysis of irreversibilities among particles suspended in a Couette device. *Journal of Rheology* **50** (2), 99–114.
- JOHNSON, S. G. 2021 The NLOpt nonlinear-optimization package.
- LYON, M. K. & LEAL, L. G. 1998*a* An experimental study of the motion of concentrated suspensions in two-dimensional channel flow. part 1. monodisperse systems. *Journal of Fluid Mechanics* **363**, 25–56.
- LYON, M. K. & LEAL, L. G. 1998*b* An experimental study of the motion of concentrated suspensions in two-dimensional channel flow. part 2. bidisperse systems. *Journal of Fluid Mechanics* **363**, 57–77.
- MAXEY, M. 2017 Simulation methods for particulate flows and concentrated suspensions. *Annual Review of Fluid Mechanics* **49**, 171–193.
- METZGER, B. & BUTLER, J. E. 2010 Irreversibility and chaos: Role of long-range hydrodynamic interactions in sheared suspensions. *Physical Review E* **82** (5), 051406.
- METZGER, B. & BUTLER, J. E. 2012 Clouds of particles in a periodic shear flow. *Physics of Fluids* **24** (2), 021703.
- METZGER, B., PHAM, P. & BUTLER, J. E. 2013 Irreversibility and chaos: Role of lubrication interactions in sheared suspensions. *Physical Review E* **87** (5), 052304.
- MIRBOD, P. & SHAPLEY, N. C. 2023 Particle migration of suspensions in a pressure-driven flow over and through a porous structure. *Journal of Rheology* **67** (2), 417–432.
- NELDER, J. A. & MEAD, R. 1965 A Simplex Method for Function Minimization. *The Computer Journal* **7** (4), 308–313.
- OLUFSEN, S. N., ANDERSEN, M. E. & FAGERHOLT, E. 2019 μ dic: An open-source toolkit for digital image correlation. *SoftwareX* **11**.
- PHAM, P., BUTLER, J. E. & METZGER, B. 2016 Origin of critical strain amplitude in periodically sheared suspensions. *Physical Review Fluids* **1** (2), 022201.
- PHAM, P., METZGER, B. & BUTLER, J. E. 2015 Particle dispersion in sheared suspensions: Crucial role of solid-solid contacts. *Physics of Fluids* **27** (5), 051701.
- PINE, D. J., GOLLUB, J. P., BRADY, J. F. & LESHANSKY, A. M. 2005 Chaos and threshold for irreversibility in sheared suspensions. *Nature* **438** (7070), 997–1000.
- RAMPALL, I., SMART, J. R. & LEIGHTON, D. T. 1997 The influence of surface roughness on the particle-pair distribution function of dilute suspensions of non-colloidal spheres in simple shear flow. *Journal of Fluid Mechanics* **339**, 1–24.
- SNOOK, B., BUTLER, J. E. & GUAZZELLI, E. 2015 Dynamics of shear-induced migration of spherical particles in oscillatory pipe flow. *Journal of Fluid Mechanics* **786**, 128–153.
- VINCENT, L. 1993 Morphological grayscale reconstruction in image analysis: applications and efficient algorithms. *IEEE Transactions on Image Processing* **2** (2), 176–201.
- ZIVKOVIC, Z. 2004 Improved adaptive Gaussian mixture model for background subtraction. In *Proceedings of the 17th International Conference on Pattern Recognition, ICPR*, vol. 2, pp. 28–31.